Visible-Light-Induced Exciton Dynamics and Trans-to-Cis Isomerization in Azobenzene Aggregates: Insights from Surface Hopping / Semiempirical Configuration Interaction Molecular Dynamics Simulations

Evgenii Titov*

University of Potsdam, Institute of Chemistry, Theoretical Chemistry, Karl-Liebknecht-Straße 24-25, 14476 Potsdam, Germany

E-mail: titov@uni-potsdam.de

Abstract

Assemblies of photochromic molecules feature exciton states, which govern photochemical and photophysical processes in multichromophoric systems. Understanding photoinduced dynamics of the assemblies requires nonadiabatic treatment involving multiple exciton states and numerous nuclear degrees of freedom, thus posing a challenge for simulations. In this work, we address this challenge for aggregates of azobenzene, a prototypical molecular switch, performing on-the-fly surface hopping calculations combined with semiempirical configuration interaction electronic structure and augmented with transition density matrix analysis to characterize exciton evolution. Specifically, we consider excitation of azobenzene tetramers in the $n\pi^*$ absorption band (located in the visible (blue) part of the electromagnetic spectrum) thus extending our

1

recent work on dynamics after $\pi\pi^*$ excitation (corresponding to the ultraviolet region) [Titov, *J. Phys. Chem. C* **2023**, *127*, 13678–13688]. We find that the $n\pi^*$ excitons, which are initially strongly localized by ground state conformational disorder, undergo further (very strong) localization during short-time photodynamics. This excited-state localization process is extremely ultrafast, occuring within first 10 fs of photodynamics. We observe virtually no exciton transfer of the localized excitons in the $n\pi^*$ manifold. However, the transfer may occur via secondary pathways involving $\pi\pi^*$ states or the ground state. Moreover, we find that $n\pi^*$ quantum yields of the *trans*-to-*cis* isomerization are reduced in the aggregated state.

1 Introduction

Chromophores assembled together, such as in molecular crystals or nanoscale assemblies, give rise to formation of molecular excitons — electronically excited states of molecular aggregates.[1–3] The molecular excitons are key players in operation of organic optoelectronic devices[4] as well as in the natural process of photosynthesis.[5] A particularly interesting situation arises if the monomer itself — the building block of a molecular aggregate — is a photochromic system. In this case, aggregation may affect not only photophysics of the chromophore (*e.g.*, electronic spectra[6]) but also its photochemistry (*e.g.*, hinder isomerization[7,8]).

A prototypical example of the photochromic system is azobenzene, undergoing *trans* $\leftrightarrow$ *cis* isomerizations upon illumination with light in ultraviolet (UV) and visible regions of the electromagnetic spectrum.[9] Arrangement of numerous azobenzene units in proximity to each other takes place in molecular crystals,[6] liquid crystals,[10] self-assembled monolayers (SAMs),[11,12] micelles of azobenzene-containing surfactants,[13,14] surfactant–polymer complexes,[15,16] and other supramolecular systems and architectures.[17,18] Distinct spectroscopic signatures (such as spectral shifts and changes in absorbance) originating from azobenzene aggregation have been observed experimentally, *e.g.*, for SAMs[19] and micellar solu-

2

tions.[14] Moreover, several studies have reported first-principles calculations of exciton states of azobenzene aggregates and SAMs.[20–25] However, these studies address exciton states for *fixed* nuclear configurations of the aggregates. To go beyond this single-geometry picture, it is necessary to account for ground-state conformational (geometrical) disorder (induced by thermal fluctuations) and excited-state dynamical effects.

The effect of the conformational disorder in the electronic ground state may be modelled either by performing ground-state molecular dynamics (GSMD) simulations (usually applying a thermostat to mimic temperature of environment) or by sampling Wigner function corresponding to the vibrational ground state of the electronic ground state.[26] The vertical absoprtion spectra and exciton localization are then computed for a set of selected geometries. In the case of large (multichromophoric) molecules or molecular aggregates, the GSMD approach is usually used, since the Wigner function is computed in practice in the harmonic approximation and, hence, the Wigner sampling may be problematic for anharmonic modes, which are present in the complex systems. Recently, we have investigated the effect of the conformational disorder on the exciton states of a model azobenzene tetramer (with *trans*-azobenzene units assembled in an H-aggregate fashion) by time-dependent density functional theory (TD-DFT) calculations perfromed at nuclear configurations generated by the GSMD DFT approach.[27] We have found that the ground-state conformational disorder leads to partial localization of the $\pi\pi^*$ excitons (with a localization degree being dependent on temperature) and strong localization (to a single monomer) of the $n\pi^*$ excitons.[27] Here we should recall that the absorption spectrum of *trans*-azobenzene includes a weak lower-energy $n\pi^*$ band and an intense higher-energy $\pi\pi^*$ band.[28,29]

Further, illumination of molecular assemblies with light excites them from the electronic ground state to the electronically excited state(s), inducing subsequent exciton dynamics. These dynamics require, in general, nonadiabatic treatment, *i.e.*, coupled electron-nuclear dynamics involving many potential energy surfaces should be described. Over the past years the exciton dynamics in multichromophoric systems have been modelled using various ap-

3

proaches to nonadiabatic dynamics, including surface hopping (SH),[30–35] multiconfiguration time-dependent Hartree (MCTDH)[36,37] and multi-layer MCTDH (ML-MCTDH),[38–40] Ehrenfest and multiconfigurational Ehrenfest (MCE),[41,42] and symmetrical quasi-classical windowing model applied to the classical Meyer–Miller vibronic Hamiltonian (SQC/MM).[43,44] However, only few studies have been devoted to the *exciton dynamics* in azobenzene aggregates. Sangiogo Gil, Persico, and Granucci used surface hopping combined with an *exciton model* to simulate Frenkel exciton dynamics in an azobenzene dimer (azobenzenophane)[45] and an azobiphenil monolayer.[46] Recently, we have employed a *supermolecule* approach to investigate exciton dynamics in several azobenzene tetramers (both free and embedded in a SAM-like environment) after $\pi\pi^*$ excitation.[47] The exciton evolution was explored using a transition density matrix analysis, allowing one to judge on spatial localization of excitons during surface hopping dynamics.[30,31,33,34,48–52]

In this work, we study the exciton dynamics after $n\pi^*$ excitation, *i.e.*, induced with visible light excitation, for the models introduced in our previous work on the photodynamics after $\pi\pi^*$ excitation.[47] While the $\pi\pi^*$ absorption band of azobenzene is more intense than the $n\pi^*$ band, the latter is located in the visible region of the electromagnetic spectrum, which is of preference for applications requiring lower energy photons, *e.g.*, for use in biological systems.[53] Indeed, one of the central goals of contemporary research in the field of photoswitches is to enable efficient isomerization with low-energy photons.[54–56] Here, using nonadiabatic dynamics simulations, we study how the corresponding low-energy excitons formed in azobenzene aggregates evolve in time.

The paper is organized as follows. In the next section (section 2) we describe the used models and methods. In section 3, we present and discuss the results. Specifically, in subsection 3.1, we describe the absorption spectrum of the aggregates and initial exciton localization. Next, in subsection 3.2, we discuss exciton dynamics initiated by $n\pi^*$ excitation. After that, excited-state lifetimes and quantum yields of the *trans* → *cis* isomerization are presented in subsection 3.3. Section 4 concludes the work.

4

2 Models and Methods

We considered the models used in our recent work.[47] Namely, these models are "free" tetramers of stacked azobenzenes differing by nearest-neighbour distance (3.5 and 5.5 Å) and "constrained" tetramers embedded in a perimeter of further azobenzene molecules, similarly to the situation realized in SAMs (these latter models are called SAMs in what follows). The SAM 5.5 Å model is shown in Fig. 1. All other studied models may be obtained from this model by changing lattice parameters and, in the case of the free tetramers, by removing the perimeter molecules. The lattice parameters are $a = 5.50$ Å and $b = 9.43$ Å for SAM 5.5 Å, and $a = 3.50$ Å and $b = 6.00$ Å for SAM 3.5 Å (the a/b ratio is the same in both cases, $a/b \approx 0.583$). The SAM models are described using a quantum mechanics/molecular mechanics (QM/MM) approach: the central tetramer (thick molecules in Fig. 1) is the QM part and the perimeter (thin) molecules form the MM part. Further visualizations of the studied systems are provided in ref. 47 (see Fig. 1 and Fig. S1 there). We also note that these models represent an extension of our earlier models based on a QM dimer.[57,58]
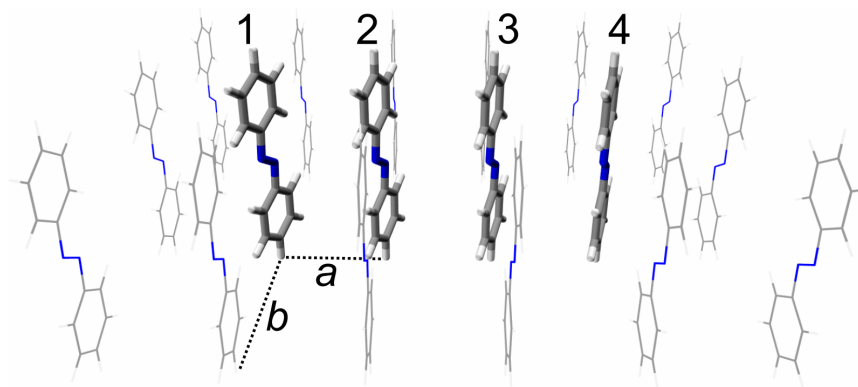
Figure 1: Model of SAM 5.5 Å. Shown is the starting geometry for the Langevin ground-state trajectory. Thick molecules are the QM part, and the thin molecules are the MM part. The numbering of the QM molecules is shown on top. The parameters of the rectangular lattice are $a = 5.50$ Å and $b = 9.43$ Å. Further models considered in this work are SAM 3.5 Å ($a = 3.50$ Å and $b = 6.00$ Å) and "free" tetramers with $a = 5.50$ Å and $a = 3.50$ Å, which are not surrounded by the thin MM molecules (formally $b = \infty$). Perspective projection is used in this figure.

To model nonadiabatic dynamics induced by visible light ($n\pi^*$) excitation we use the

approach applied in ref. 47 to study relaxation after UV ($\pi\pi^*$) excitation. In this approach, the electronic structure of the QM tetramer is modeled with configuration interaction singles (CIS) based on molecular orbitals (MO) obtained from a self-consistent field calculation with floating occupation (FO) numbers[59] using the Austin Model 1 (AM1)[60] that was reparameterized (r) for azobenzene.[61] The method is abbreviated as rAM1/FOMO-CIS in what follows. For the CIS calculations, a restricted active space of eight highest occupied (HO) and four lowest unoccupied (LU) (also referred to as virtual) MOs was used. This active space includes orbitals originating from HOMO−1 (π), HOMO (n), and LUMO (π^*) of a monomer (the orbitals are shown in Fig. S2 of ref. 47). In total, 65 Slater determinants are used to construct electronic wave functions.

In addition, to better describe noncovalent interactions, van der Waals (vdW) interaction terms, described with the Lennard-Jones potential, are added between atoms of different monomers (3456 pairwise potentials in total, for the QM part).[62] The atomic vdW parameters were taken from the OPLS-AA force field.[63] The parameters for atom pairs were calculated taking a geometric mean of the atomic parameters. The used atomic parameters are σ_C = 3.55 Å, σ_H = 2.42 Å, σ_N = 3.25 Å, ϵ_C = 0.07 kcal/mol, ϵ_H = 0.03 kcal/mol, ϵ_N = 0.17 kcal/mol. The MM part of the SAM models interacts with the QM part by the same vdW interaction. Moreover, the MM molecules were kept fixed during molecular dynamics (MD) simulations. In addition, for the QM part (for all models), the C and H atoms in *para*-position on one end (two atoms per monomer) were kept fixed, imitating mounting to a surface.

To sample initial conditions for surface hopping simulations, ground-state Langevin MD trajectories at T = 300 K from ref. 47 were used. For each system, the geometries and velocities were selected from these 20 ps long trajectories every 100 fs, starting at 5 ps, which results in 151 initial conditions per system. In comparison to ref. 47, we (almost) doubled the number of trajectories to improve statistics when averaging over a swarm of trajectories (76 initial conditions were used before[47]). We should note here that computation time per

6

trajectory could be reduced by considering less electronic states, since $n\pi^*$ states are located lower in energy than the $\pi\pi^*$ states (see below).

The vertical absorption spectra were then calculated for the selected geometries using rAM1/FOMO-CIS, and the obtained stick spectra were broadened as:

$$I(E) = \frac{1}{N_{sn}} \sum_{\alpha=1}^{N_{sn}} \sum_{i=1}^{N_{st}} f_{i,\alpha} \exp\left(-\frac{1}{2\gamma^2}(E - E_{i,\alpha})^2\right) \tag{1}$$

Here, I is intensity, E is excitation energy, $N_{sn} = 151$ is the number of selected snapshots, $N_{st} = 20$ is the number of excited singlet states, $E_{i,\alpha}$ and $f_{i,\alpha}$ are the excitation energy and oscillator strength, respectively, for the $S_0 \rightarrow S_i$ transition, for snapshot α, and $\gamma = 0.18598$ eV (1500 cm^{-1}) is a broadening parameter (the same value as used in ref. [47]). The brightest state among the $n\pi^*$ states (S_1–S_4) was selected as the initial state for the surface hopping calculations. We should recall here that the monomeric $S_0 \rightarrow S_1$ transition is dark for the ground-state minimum geometry, but it acquires nonzero (albeit small) oscillator strength upon geometric distortions resulting from ground-state MD simulations in our case.[64] In the tetramer, the $n\pi^*$ monomeric state (S_1) is split into four states, S_1–S_4. Comparing oscillator strengths of the transitions to these exciton states from the ground state of the tetramer (for a given initial geometry), we select the state with the highest oscillator strength as an initial state for a surface hopping run.

The nonadiabatic dynamics were modeled using the trajectory surface hopping approach[65] combined with the semiempirical configuration interaction method,[66] namely rAM1/FOMO-CIS introduced above. The SH trajectories were propagated for 10 ps with a time step of 0.1 fs. The energy-based decoherence correction[67] was used to remedy overcoherence of the original surface hopping algorithm (with constant $C = 0.1$ hartree; see Eq. (17) in Ref. [67]). The time-dependent electronic wave function was propagated using the local diabatization scheme.[48,66] The nuclei were propagated classically on the on-the-fly calculated adiabatic rAM1/FOMO-CIS PESs. The hopping probabilities were calculated using the prescription

7

by Granucci and co-authors described in the appendix of ref. [68]. We note that the local diabatization scheme is suited to propagate the electronic wave function in the presense of trivial crossings occuring for multichromophoric systems with excitonically weakly coupled states.[69,70] However, there is no unique way to calculate hopping probabilities in the framework of local diabatization,[70,71] and the accuracy of population dynamics may depend on the way the hopping probabilities are calculated.[71] Nine lowest singlet states (S_0–S_8) were included in the SH simulations. Apart from the ground state (S_0) and the $n\pi^*$ states (S_1–S_4) we also include the $\pi\pi^*$ states S_5–S_8 originating from the monomeric S_2 state to allow for upward $n\pi^* \to \pi\pi^*$ nonadiabatic transitions and to check if the $\pi\pi^*$ states play a role in photodynamics induced with visible light ($n\pi^*$ excitation).

In all MD simulations we used the so-called added potential (added to each of the four molecules of the tetramer) which corrects the low AM1 N-inversion barriers and phenyl rotations about the N–C bonds.[61] The state-specific corrections developed in Ref. [61] were not used, since they were derived specifically for monomeric adiabatic states.

Adiabatic electronic state populations were computed as fractions of trajectories being in the state of interest. The quantum yield Φ was computed as the ratio of the number of the reactive trajectories (*i.e.*, those undergoing *trans* $\to$ *cis* isomerization) to the number N_t of trajectories that reached the ground state within 10 ps. The standard error was calculated as the standard deviation of the sample proportion, $\Delta\Phi = \sqrt{\Phi(1-\Phi)/N_t}$. The reactive trajectories were identified monitoring the change in the CNNC dihedral angles from $\sim 180°$ to $\sim 0°$.

The exciton dynamics were traced using the transition density matrix (TDM) analysis presented in our previous work.[47] Below we recount this analysis for completeness. The reduced one-particle spinless TDM is defined as:[72]

$$\rho^{0I}(\vec{r}, \vec{r}') = N \iint \cdots \int \left[\Psi^0(\vec{x}, \vec{x}_2, \ldots, \vec{x}_N) \Psi^I(\vec{x}', \vec{x}_2, \ldots, \vec{x}_N) \right]_{\sigma' \to \sigma} d\vec{x}_2 \ldots d\vec{x}_N d\sigma \qquad (2)$$

8

Here, Ψ^0 is the ground state electronic wave function and Ψ^I is the excited current (active) state electronic wave function, $\vec{x}$ collects spatial $\vec{r}$ and spin σ variables of an electron, and N is the number of electrons. We note that the electronic wave functions depend parametrically on the nuclear coordinates $\mathbf{R}(t)$ (which, in turn, depend on time in quantum–classical trajectory-based methods), but we do not write explicitly this dependence for the sake of brevity. We also assume the wave functions to be real.

The electronic, adiabatic wave functions are linear combinations of the unexcited and singly excited Slater determinants Φ_K:

$$\Psi^{0/I}(\mathbf{x}) = \sum_K C_K^{0/I} \Phi_K(\mathbf{x}) \tag{3}$$

Here, $\mathbf{x}$ collects the variables of all electrons.

Substitutig (3) into (2), one can rewrite the TDM as an expansion in MO products, and further expressing MOs φ_i as linear combinations of atomic orbitals (AOs) η_μ, $\varphi_i(\vec{r}) = \sum_\mu c_{\mu i}\eta_\mu(\vec{r})$, as an expansion in AO products:

$$\begin{aligned}
\rho(\vec{r}, \vec{r}') &= N \sum_{K,L} C_K^0 C_L^I \iint \cdots \int [\Phi_K \Phi_L]_{\sigma' \to \sigma}\, d\vec{x}_2 \ldots d\vec{x}_N d\sigma \\
&= \sum_{i,j} P_{ij}^{[\mathrm{MO}]} \varphi_i(\vec{r}) \varphi_j(\vec{r}') \\
&= \sum_{\mu,\nu} P_{\mu\nu}^{[\mathrm{AO}]} \eta_\mu(\vec{r}) \eta_\nu(\vec{r}')
\end{aligned} \tag{4}$$

Here, $\mathbf{P}^{[\mathrm{MO}]}$ and $\mathbf{P}^{[\mathrm{AO}]}$ are TDMs in MO and AO basis, respectively. In our case, the $\mathbf{P}^{[\mathrm{MO}]}$ matrix has a size of 12×12 (since there are 8 occupied and 4 virtual orbitals in the active space), and the $\mathbf{P}^{[\mathrm{AO}]}$ matrix 264×264 (the applied semiempirical method uses 264 AOs to describe the electronic structure of the tetramer).

Further, we contract the $\mathbf{P}^{[\mathrm{AO}]}$ matrix to monomers[73,74] (denoted with X, Y) by computing the "fraction of transition density matrix" (FTDM) matrix $\mathbf{F}$:[22]

$$F_{XY} = \frac{\sum\limits_{\mu \in X} \sum\limits_{\nu \in Y} \left(P_{\mu\nu}^{[AO]} \right)^2}{\sum\limits_{\mu \in \text{tetramer}} \sum\limits_{\nu \in \text{tetramer}} \left(P_{\mu\nu}^{[AO]} \right)^2} \qquad (5)$$

The diagonal elements F_{XX} quantify contributions of local excitations and off-diagonal elements F_{XY}, $Y \neq X$ charge-transfer excitations. For a tetramer, the **F** matrix has a size of 4×4.

Using the elements of the **F** matrix, we compute the participation number (PN) following the prescription of ref. 75 (there the quantity is called "delocalization length" (DL)):

$$PN = \frac{1}{\sum\limits_{X} \left(\sum\limits_{Y} \frac{F_{XY} + F_{YX}}{2} \right)^2} \qquad (6)$$

PN is a *scalar* ranging from 1 (complete exciton localization) to 4 (complete exciton delocalization). We note that the quantity given by eq. (6) (or equations of a similar form) is sometimes called "inverse participation ratio (IPR)",[73,76,77] as was also done in our previous works.[27,47] However, as recently highlighted by Herbert,[78] the term IPR may lead to a confusion. Indeed, following ref. 79, complete localization corresponds to a participation ratio (PR) of $1/n$, and IPR $\equiv 1/PR = n$ (with n being the number of monomers), whereas for complete delocalization PR = 1 (and IPR = 1 as well). On the other hand, according to Scholes,[80] localization corresponds to IPR = 1 and delocalization to IPR = $1/n$, and the delocalization length is given by DL = 1/IPR. Moreover, comparing the definition of PR given by Bell[81] to the definition of IPR by Thouless,[82] one can see that IPR $\neq 1/PR$, instead PR·IPR = $1/n$ (see also ref. 83). [It should be noted though that Thouless[82] referred to the definition given by Bell and Dean in ref. 84 that differs from that in ref. 81 by a factor of $1/n$, thus leading to PR·IPR = 1 (see also eqs. (3) and (4) in ref. 85).] Therefore, following Tretiak and co-workers,[86] we will call the quantity defined by eq. (6) "participation number" (or "PN") to avoid possible confusions associated with the "IPR".

10

We also compute overall measures of local excitations (LE) and charge transfer (CT) as:

$$\mathrm{LE} = \sum_X F_{XX} \tag{7a}$$

$$\mathrm{CT} = \sum_{X \neq Y} F_{XY} \tag{7b}$$

In addition, we introduce highest (H), intermediate (H$-$1 and L+1), and lowest (L) monomers through sorting the FTDM diagonal, $F_{\mathrm{H}} > F_{\mathrm{H}-1} > F_{\mathrm{L}+1} > F_{\mathrm{L}}$, allowing one to judge on exciton localization on single geometry level (for excitons dominated by local excitations).[27,33,87] The FTDM and derived quantities (PN, LE, and CT) are calculated along surface hopping trajectories, $i.e.$, these quantities depend on $\mathbf{R}(t)$. Finally, averaging over a swarm of trajectories (for a given system) is performed.

The monomer dynamics were modeled using rAM1/FOMO-CIS with an active space consisting of HOMO$-$1 (π), HOMO (n), and LUMO (π^*). Three electronic states (S_0, S_1, and S_2) were taken into account, and all 151 trajectories were launched from the S_1 ($n\pi^*$) state.

The rAM1/FOMO-CIS calculations were done with the development version of MOPAC 2002.[88] The TINKER package was used to handle QM/MM interactions.[89]

3 Results and Discussion

3.1 Absorption Spectrum and Initial Exciton Localization

The electronic absorption spectra of the models calculated using eq. (1) are shown in Fig. 2. These spectra are very similar to those shown in Fig. 2 of ref. 47 (as expected), but now they are calculated using 151 geometries (per system) instead of 76 used in the previous work.[47] In the present work, we are concerned with dynamics induced by visible light excitation. Therefore, the $n\pi^*$ absorption band, located between 2.0 and 3.3 eV (Fig. 2, left) is of a

11

particular interest here.
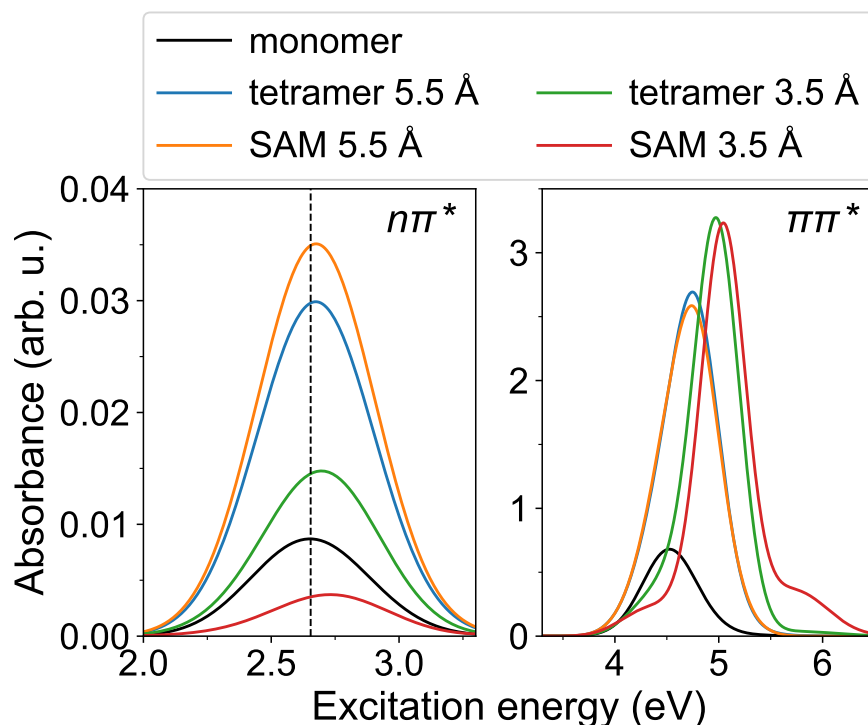
Figure 2: Broadened absorption spectra calculated at the geometries selected from the ground-state Langevin trajectories (151 geometries per system). The $n\pi^*$ band is shown on the left, and the $\pi\pi^*$ band on the right.

As already mentioned above, the $n\pi^*$ transition of the monomer (the $S_0 \rightarrow S_1$ transition) is forbidden for the optimized *trans* ground-state geometry processing the C_{2h} symmetry.[90] However, the transition acquires some intensity via coupling to vibrations[64] and is well observed in experiments.[28,29] Since the transition dipole moment is zero at the equilibrium geometry, it is not possible to predict the changes in excitation energy and oscillator strength upon aggregation using the molecular exciton theory[2] for the $n\pi^*$ transition (assuming identical, C_{2h} geometries of the monomers).

Based on the Langevin, ground-state MD simulations, we observe that the $n\pi^*$ bands of the tetrameric models are slightly blue-shifted with respect to the monomer, by ~0.02 eV for models with $a = 5.5$ Å, ~0.04 eV for tetramer 3.5 Å, and ~0.08 eV for SAM 3.5 Å. Interestingly, larger absorbance is observed for models with $a = 5.5$ Å in comparison to

those with $a = 3.5$ Å. This effect is opposite to what is seen for the strong $\pi\pi^*$ band in the UV region (Fig. 2, right). We note that in the simple exciton model (considering an H-aggregate composed of identical monomer geometries with the same non-zero transition dipole moment), a larger enhancement should occur for a smaller separation distance owing to a larger exciton splitting.[25] As discussed previously for the dimeric models,[57] the trend in absorbance observed for the $n\pi^*$ band upon aggregation is determined by the extent of deviation of the monomers forming an aggregate from the equilibrium, planar C_{2h} geometry. To quantify this deviation, we computed the NNCC dihedral angles of the monomers for the studied models, for the snapshots selected from the ground-state trajectories (see Tab. S1). The mean NNCC dihedral angles and the corresponding standard deviations decrease in the order SAM 5.5 Å / tetramer 5.5 Å > tetramer 3.5 Å > SAM 3.5 Å, which correlates with the decrease in the $n\pi^*$ absorbance in this order (Fig. 2, left).

Further, the brightest among the $n\pi^*$ states was selected as an initial electronic state for a surface hopping trajectory. In Fig. 3, left, the distributions of initial adiabatic states are shown. As can be seen, any of the lowest four excited states can be the brightest state depending on an aggregate geometry. The distributions are qualitatively close to the uniform one. Numerically, we find the highest fractions of 0.31 S_3 for tetramer 5.5 Å, 0.32 S_1 for SAM 5.5 Å, 0.28 S_3 for tetramer 3.5 Å, and 0.34 S_4 for SAM 3.5 Å. These "quasi-uniform" distributions are in contrast to the situation realized for the $\pi\pi^*$ excitation, where the S_8 state is almost always the brightest state.[47]

13
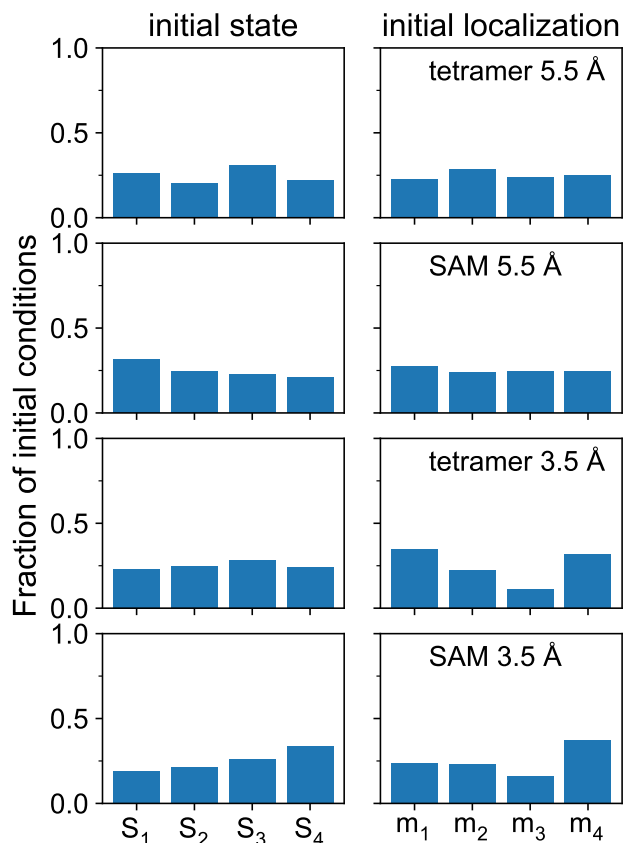
Figure 3: Left column: Distributions of initial adiabatic states, which are selected as the brightest states among the $n\pi^*$ ones. Right column: Distributions of initially excited monomers; "m_i" stands for "monomer i" with $i = 1, 2, 3, 4$ (see Fig. 1 for numbering of the monomers).

Furthermore, the $n\pi^*$ states are strongly localized, *i.e.*, an excitation involves only one monomer, as can be seen in Tab. 1, where we list ensemble-averaged values of PN and F_{H} calculated at the snapshots from the ground-state trajectories, *i.e.*, for the initial conditions for the SH trajectories ($t = 0$). The PN($t = 0$) values range between ~ 1.02 and ~ 1.07, and the $F_{\text{H}}(t = 0)$ values between ~ 0.97 and ~ 0.99. The degree of the initial localization decreases in the order SAM 5.5 Å > tetramer 5.5 Å > tetramer 3.5 Å > SAM 3.5 Å. The strong localization of the brightest $n\pi^*$ excitons is in agreement with the results of our earlier DFT/TD-DFT study (the TD-DFT PN ≈ 1.1 and $F_{\text{H}} \approx 0.97$ for tetramer 3.5 Å at $T \approx 300$ K).[27]

14

Table 1: Initial values of the participation number $\mathrm{PN}(t = 0)$ and the largest diagonal element of FTDM $F_\mathrm{H}(t = 0)$ averaged over the swarm of initial geometries (151 per system).

system	$\mathrm{PN}(t = 0)$	$F_\mathrm{H}(t = 0)$
tetramer 5.5 Å	1.028	0.988
SAM 5.5 Å	1.020	0.991
tetramer 3.5 Å	1.061	0.972
SAM 3.5 Å	1.072	0.967

The initial localization can occur on any of the four monomers of a tetramer as shown in Fig. 3, right, where we plot distributions for initial localization. To do so, the diagonal of the FTDM ($\mathbf{F}$) matrix is considered to identify the monomer bearing the highest F_{XX} value (at a given aggregate geometry). Considering an ensemble of the initial conditions, we count how many times monomer X (m_X) traps the exciton. As can be seen in Fig. 3, right, the localization distributions are qualitatively more uniform for the the models with $a = 5.5$ Å than for the models with $a = 3.5$ Å. Quantitaively, we find the largest fractions of 0.28 m_2 for tetramer 5.5 Å, 0.27 m_1 for SAM 5.5 Å, 0.34 m_1 for tetramer 3.5 Å, and 0.37 m_4 for SAM 3.5 Å.

3.2   Exciton Dynamics

The surface hopping MD simulations were performed starting in the brightest $n\pi^*$ adiabatic state, thus modeling nonadiabatic relaxation after excitation with visible light. The evolution of the ensemble-averaged PN in time is shown in Fig. 4. The left panel shows the whole simulation period of 10 ps, whereas the right panel zooms into the first 20 fs. As already described in the previous subsection, the initial excitons are strongly localized, with the PN values at $t = 0$ being less than 1.1. Remarkably, during the short-time dynamics ($t < 10$ fs) the excitons become even more localized as can be seen from the right panel of Fig. 3, with the PN values approaching $\sim$1.00. Using a simple exponential fit of the form

$$\mathrm{PN}(t) = A \exp(-t/\tau_\mathrm{loc}) + C \tag{8}$$

15

(applied to the first 20 fs of the simulations) we obtain the exciton localization time constants τ_{loc} presented in the right column of Tab. 2. These time constants amount to $\sim$6–7 fs, which means extremely ultrafast further localization (of initially quite strongly localized $n\pi^*$ excitons) originating from the short-time excited-state dynamics. The fits obtained using eq. (8) are also shown in the right panel of Fig. 4. We should note that the fits do not reproduce the details of the PN curves obtained from the numerical simulations, but they allow as to obtain a characteristic time of the extremely ultrafast localization process occurring during excited-state dynamics.
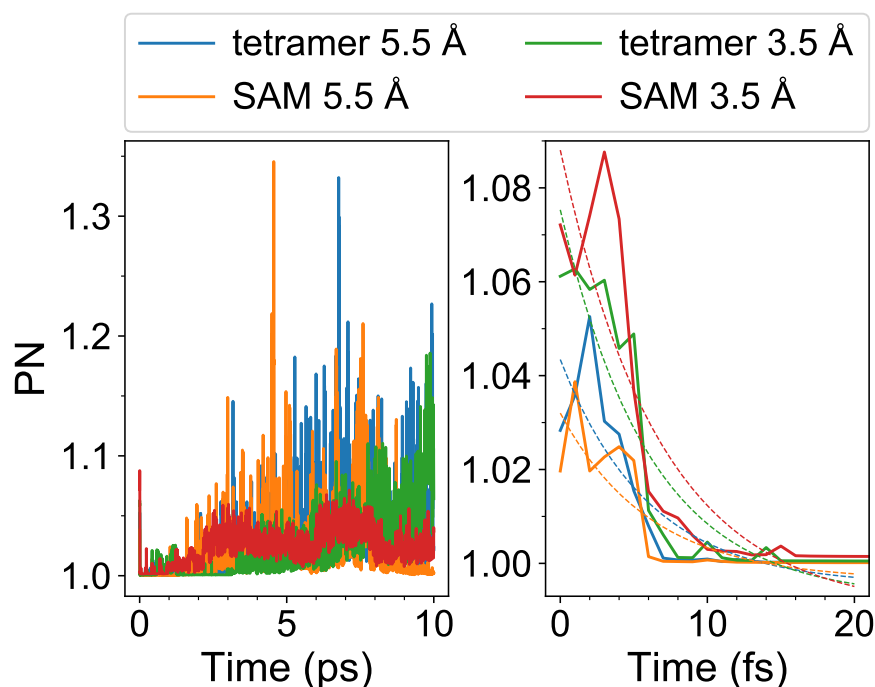
Figure 4: Evolution of the participation number (PN) for the whole simulation period of 10 ps (left) and for the first 20 fs (right) for the studied tetrameric models. The dashed lines in the right panel are the exponential fits defined by Eq. (8).

Table 2: Time constants for the studied systems.

system	$\tau_{n\pi^*}$ (fs)	τ_{S_0} (fs)	τ_{loc} (fs)
monomer	1266	1266	—
tetramer 5.5 Å	2366	2712	6.0
SAM 5.5 Å	1913	2050	6.1
tetramer 3.5 Å	5890	6235	6.0
SAM 3.5 Å	18748	20305	6.8

16

Further, time evolution of F_{XX} diagonal matrix elements, highest-to-lowest FTDM values ($F_{H/H-1/L+1/L}$), PN, CT, and active adiabatic electronic state for typical *single* trajectories of the studied systems is shown in Fig. 5, for the first 20 fs of dynamics. For the shown trajectories, the initial electronic state is either S_3 or S_4 (see the last row of Fig. 5). However, the internal conversion to the S_1 state takes only $\sim$5 fs. The initial exciton is strongly localized on a single fragment — $X = 1$ for all systems except tetramer 3.5, for which $X = 3$ in the given case. The initial localization is transiently perturbed during internal conversion, but subsequently recovered, and the exciton stays localized while the aggregate evolves in the S_1 state. We note that no exciton transfer occurs during the short-time dynamics, *i.e.*, the same fragment X bears exciton at $t = 0$ and $t = 20$ fs (for the same trajectory). [For few trajectories the short-time exciton transfer is observed as exemplified in Fig. S1.] The transient localization perturbation / delocalization is logically reflected in the PN curves, which deviate from 1 at corresponding times (see the third row of Fig. 5). This behavior correlates with the non-monotonic, short-time evolution of the ensemble-averaged PN curves shown in Fig. 4, right. At that, the excitons are composed of local excitations, and CT ≈ 0 (and, hence, LE ≈ 1) throughout the shown time interval, see the fourth row of Fig. 5.

17
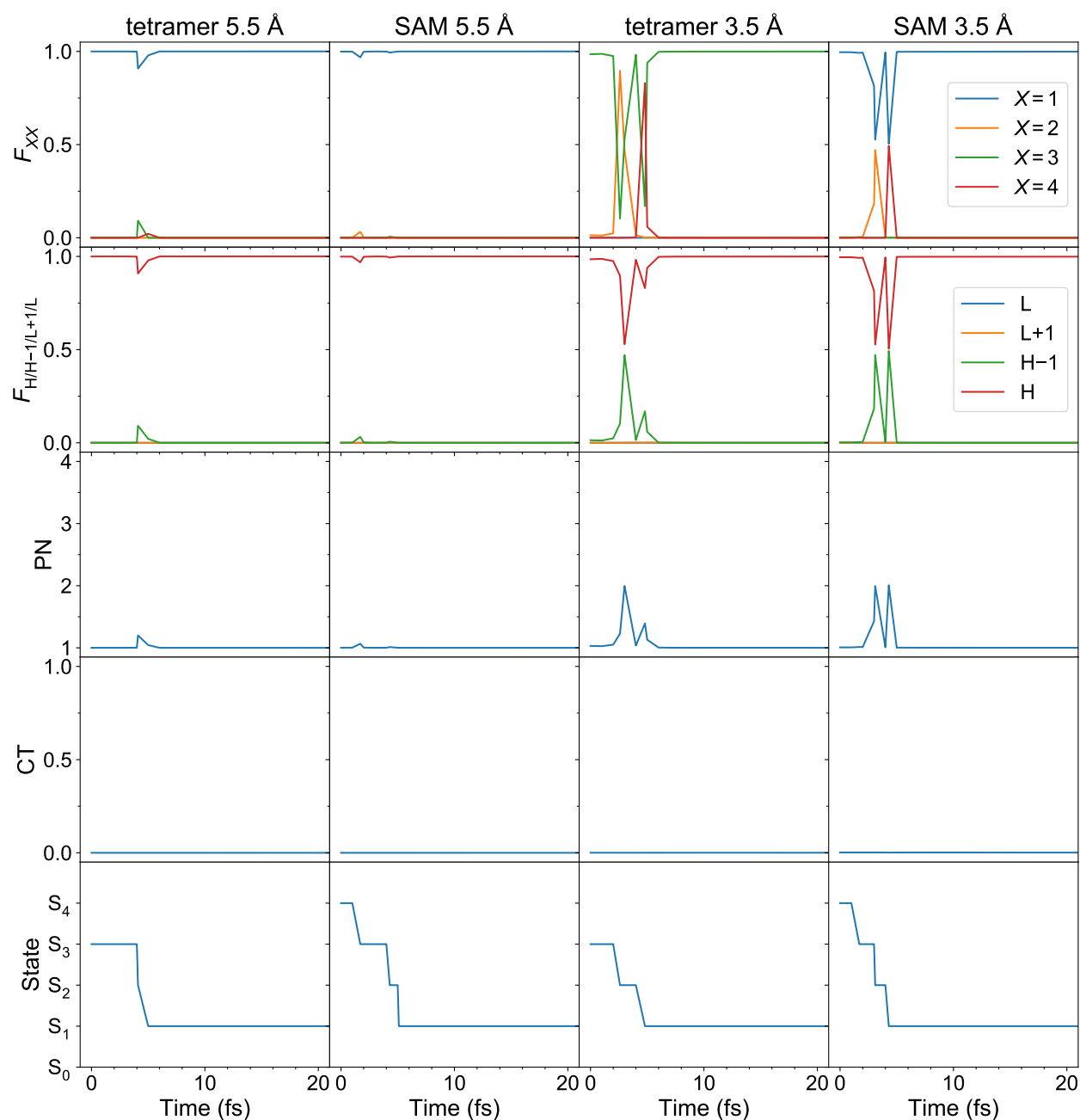
Figure 5: Evolution of F_{XX} ($X = 1, 2, 3, 4$), $F_{\mathrm{H/H-1/L+1/L}}$, PN, CT, and the active electronic state for selected single trajectories of all considered tetrameric models.

Further, at longer times the PN curves become more "noisy" and reach larger values (Fig. 4, left), with the following maxima: $\mathrm{PN_{max}} \approx 1.33$ (6767 fs) for tetramer 5.5 Å, $\mathrm{PN_{max}} \approx 1.35$ (4560 fs) for SAM 5.5 Å, $\mathrm{PN_{max}} \approx 1.19$ (9875 fs) for tetramer 3.5 Å, and $\mathrm{PN_{max}} \approx 1.07$ (7108 fs) for SAM 3.5 Å. To understand this behavior, we computed the

18

PN curves separately for the $n\pi^*$ and $\pi\pi^*$ manifolds, *i.e.*, averaging (at time t) only over trajectories residing in the corresponding manifold at time t. We note that the $\pi\pi^*$ states located above the $n\pi^*$ states are slightly populated in the course of the nonadiabatic dynamics (see Fig. 7 in next subsection). The $n\pi^*$ and $\pi\pi^*$ PN curves are shown in Fig. 6. It is seen that the $n\pi^*$ curves are close to 1 at all times (Fig. 6, left column). Quantitatively, the $n\pi^*$ PN values are $< 1.09 \, \forall \, t$ for all the models, and the temporal mean (over time of 10 ps) $n\pi^*$ PN values are 1.0007, 1.0004, 1.0010, and 1.0018 for tetramer 5.5 Å, SAM 5.5 Å, tetramer 3.5 Å, and SAM 3.5 Å, respectively. The $\pi\pi^*$ PN curves, on the other hand, extend up to PN ≈ 4 (Fig. 6, right column), with the temporal mean values of 1.14, 1.15, 1.60, and 2.08 for tetramer 5.5 Å, SAM 5.5 Å, tetramer 3.5 Å, and SAM 3.5 Å, respectively. Thus, the longer time behavior of the overall PN curves (Fig. 4, left) arises from the interplay of the strongly localized $n\pi^*$ states and more delocalized $\pi\pi^*$ states.
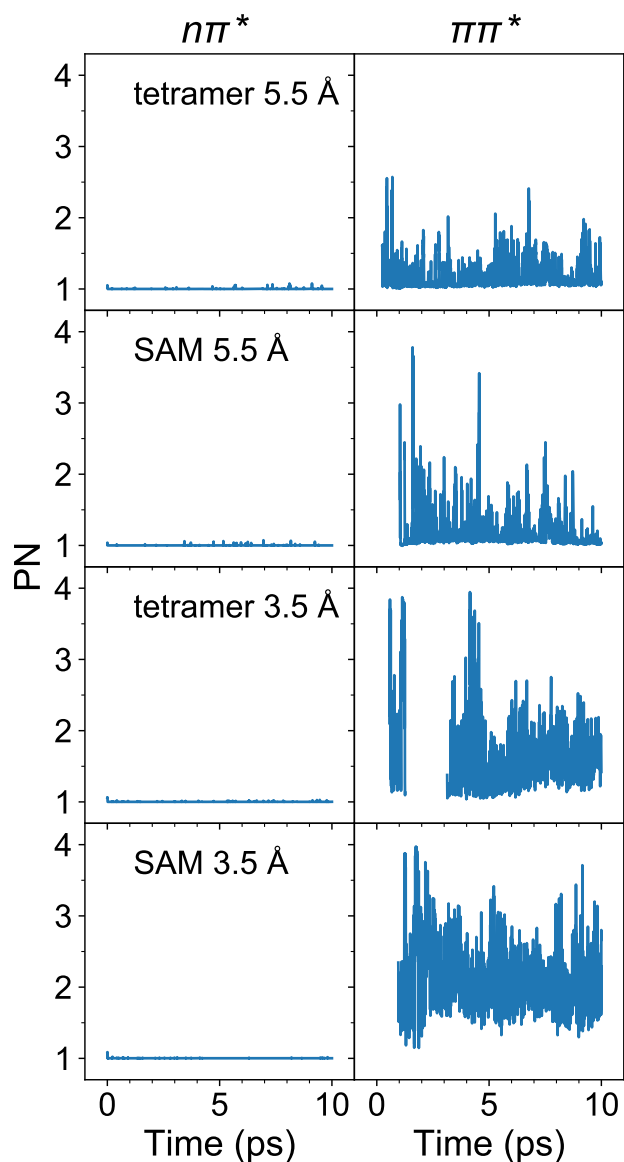
Figure 6: Participation numbers (PN) for $n\pi^*$ (left) and $\pi\pi^*$ (right) excitons.

Next, considering the entire simulation period of 10 ps, we find virtually no exciton transfer (at longer times) while the systems evolve in the $n\pi^*$ manifold. There are only three trajectories demonstrating the opposite (see Fig. S2). The very rare occurrence of the $n\pi^*$ exciton transfer is in agreement with our previous simulations of the $\pi\pi^*$ dynamics (where the $n\pi^*$ states are reached via internal conversion from the $\pi\pi^*$ states).[47] Moreover, it agrees with the previous simulations of Sangiogo Gil, Persico, and Granucci based on an exciton model.[46] However, for some trajectories the exciton transfer occurs via $n\pi^* \to \pi\pi^* \to n\pi^*$ or

20

$n\pi^* \to S_0 \to n\pi^*$ pathways (see Fig. S3). These pathways involve upward hops that require a certain amount of kinetic energy to occur, since the change in the potential energy caused by the hop should be compensated to conserve the total energy. In this respect we note that there is no energy dissipation to environment in our models; therefore, the upward hops are facilitated in the present simulations.

Lastly, there is virtually no participation of charge-transfer excitations during the dynamics initiated in the $n\pi^*$ states, as already discussed for the short-time dynamics above. In fact, we find CT ≈ 0 and LE ≈ 1 throughout the whole simulation period of 10 ps for all systems (Fig. S4). For $a = 3.5$ Å, especially for SAM 3.5 Å, there is a clear difference to the dynamics initiated in the $\pi\pi^*$ manifold, for which CT plays a bigger role (*cf.* Fig. 5 of ref. 47). For $a = 5.5$ Å, the situation is similar for both $n\pi^*$- and $\pi\pi^*$-initiated dynamics, with CT ≈ 0 and LE ≈ 1 throughout the entire simulation period (*cf.* Fig. S6 of ref. 47).

3.3 Excited-State Lifetimes and Quantum Yields of Trans-to-Cis Isomerization

The electronic state populations are shown in Fig. 7. The $n\pi^*$ manifold comprises states S_1–S_4 and the $\pi\pi^*$ manifold S_5–S_8 of the tetrameric models. For the monomer, $n\pi^*$ includes S_1, and $\pi\pi^*$ S_2.
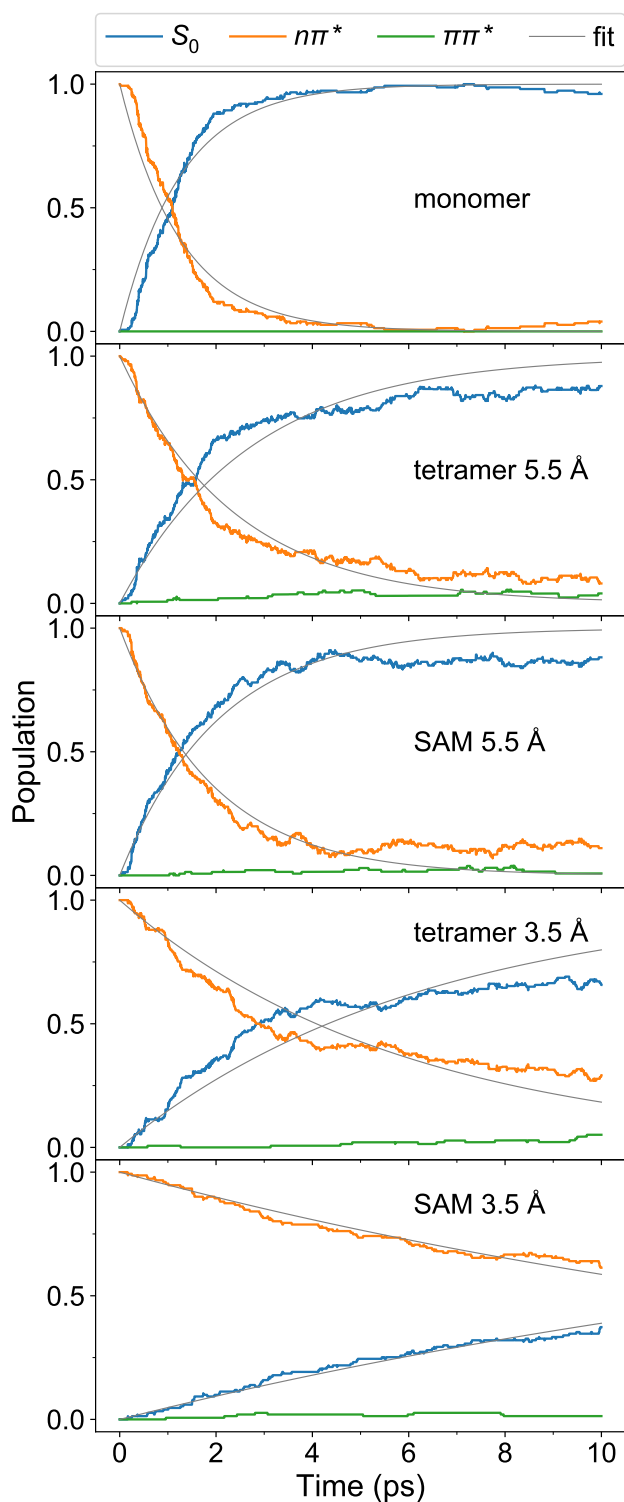
Figure 7: Populations of the S_0, $n\pi^*$, and $\pi\pi^*$ states for the studied systems. The grey lines show exponential fits defined in Eq. (9).

The $n\pi^*$ and S_0 population curves were fitted using simple mono-exponential decay

model:

$$P_{n\pi^*} = e^{-t/\tau_{n\pi^*}} \tag{9a}$$

$$P_{S_0} = 1 - e^{-t/\tau_{S_0}} \tag{9b}$$

The fitted curves are shown as thin gray lines in Fig. 7, and the corresponding time constants $\tau_{n\pi^*}$ and τ_{S_0} are listed in Tab. 2. For the monomer, we find the $n\pi^*$ lifetime $\tau_{n\pi^*}$ of $\sim$1.3 ps. This lifetime is longer than that calculated by Cantatore, Granucci, and Persico, $\sim$0.4 ps, using rAM1/FOMO-CI with more active orbitals and multiple excitations.[91] Thiel and co-workers have obtained a similar lifetime of $\sim$0.3 ps from OM2/MRCI SH simulations.[92] Zhu and co-workers have calculated a lifetime of $\sim$0.8 ps using global switching surface hopping and state-averaged CASSCF[93] In contrast, a much longer lifetime of $\sim$6 ps was reported by Martínez and co-workers based on FOMO-hh-TDA AIMS simulations.[94] (We note though that the result seems to be very sensitive to the electronic temperature,[95] as the same authors previously found a lifetime of $\sim$0.2 ps using nominally the same method[96]). In any case, we will use the $\sim$1.3 ps to compare with, since the calculations for the tetrameric models are performed using CIS on supermolecular orbitals originating from the three orbitals of the monomer (HOMO-1, HOMO, and LUMO). We also note that the time constant for the ground state recovery, τ_{S_0}, is the same as the $n\pi^*$ excited state lifetime (Tab. 2), since the $\pi\pi^*$ state of the monomer is not populated during the dynamics (at the present level of theory), see Fig. 7, top.

For the tetrameric models, the $n\pi^*$ lifetimes are prolonged, moderately for models with $a = 5.5$ Å ($\sim$2.4 ps for tetramer 5.5 Å and $\sim$1.9 ps for SAM 5.5 Å), stronger for tetramer 3.5 Å ($\sim$5.9 ps), and the most for SAM 3.5 Å ($\sim$18.7 ps). The long $n\pi^*$ lifetime for tightly packed SAM 3.5 Å is in qualitative agreement with previous simulations of azobenzene-containing SAMs.[46,97] At that, the internal conversion to the S_1 state is extremely fast for all studied models — S_1 is populated almost completely within $\lesssim$10 fs (see Fig. S5). This result may

23

be expected since the $n\pi^*$ exciton splittings are small, and it is again in agreement with ref. 46, where the population transfer to the S_1 state for a model of 12 QM molecules occurs within 40 fs.

Further, for the tetrameric models we observe that the $\pi\pi^*$ states are slightly populated during dynamics. As a result of strong exciton splitting for the $\pi\pi^*$ states, the lowest $\pi\pi^*$ state is closer to the $n\pi^*$ states than in the monomer case, thus leading to a smaller energy gap between $n\pi^*$ and $\pi\pi^*$ manifolds. The population of the $\pi\pi^*$ states is responsible for ground-state return time constants (τ_{S_0}) being longer than the $n\pi^*$ excited state lifetimes ($\tau_{n\pi^*}$) (for a given tetrameric system), see Tab. 2. Namely, we find τ_{S_0} of $\sim$2.7 ps, $\sim$2.1 ps, $\sim$6.2 ps, and $\sim$20.3 ps for tetramer 5.5 Å, SAM 5.5 Å, tetramer 3.5 Å, and SAM 3.5 Å, respectively. Moreover, the population of the $\pi\pi^*$ states may lead to the $n\pi^* \rightarrow \pi\pi^* \rightarrow n\pi^*$ exciton transfer pathway as discussed above (see Fig. S3).

Lastly, we computed the qunatum yields of the *trans* $\rightarrow$ *cis* isomerization (see Tab. 3). In this work, we simulated 151 trajectories for each of the studied systems, whereas only 76 trajectories per system were simulated in our previous work on the $\pi\pi^*$-initiated dynamics (except for tetramer 5.5 Å, for which additional 75 trajectories were run in ref. 47 to check the effect of enlargement of the ensemble on the quantum yield). In Tab. 3 we report $n\pi^*$ (this work) and $\pi\pi^*$ (ref. 47) quantum yields for batches of 76 trajectories and 151 trajectories (for the latter, in the case of the $\pi\pi^*$ excitation, only for the monomer and tetramer 5.5 Å). [In this work, we performed additional calculations for the monomer to calculate the $\pi\pi^*$ quantum yield based on 151 trajectories.]

24

Table 3: Quantum yields $\Phi \pm \Delta\Phi$ (in %) of the *trans* $\to$ *cis* isomerization after $n\pi^*$ and $\pi\pi^*$ excitations for the studied systems, for the 151 trajectories batch (left) and the 76 trajectories batch (right). The number of trajectories which reached the ground state (N_t) is shown in parentheses.

system	151 trajectories		76 trajectories	
	$n\pi^*$	$\pi\pi^*$	$n\pi^*$	$\pi\pi^*$
monomer	13.9 ± 2.8 (151)	10.7 ± 2.5 (149)	18.4 ± 4.4 (76)	14.7 ± 4.1 (75)[a]
tetramer 5.5 Å	8.3 ± 2.3 (144)	4.1 ± 1.8 (123)[a]	5.6 ± 2.7 (71)	5.1 ± 2.9 (59)[a]
SAM 5.5 Å	7.1 ± 2.2 (141)	—	6.9 ± 3.0 (72)	4.9 ± 2.8 (61)[a]
tetramer 3.5 Å	8.1 ± 2.4 (135)	—	7.1 ± 3.1 (70)	4.6 ± 2.6 (65)[a]
SAM 3.5 Å	0 (80)	—	0 (41)	0 (66)[a]

[a] From ref. 47.

First of all, comparing within a given batch (76 or 151 trajectories), we see that the $n\pi^*$ quantum yield is higher than the $\pi\pi^*$ quantum yield, namely $\sim$14% vs. $\sim$11% (151 trajectories) and $\sim$18% vs. $\sim$15% (76 trajectories). While this is correct qualitatively, we see that the $n\pi^*$ quantum yield is only 1.2–1.3 times larger than the $\pi\pi^*$ quantum yield instead of a known factor of $\sim$2.[94,98] In this respect, we note that in this work we use FOMO-CIS, *i.e.*, only single excitations within an active space of HOMO$-$1, HOMO, and LUMO are taken into account. To reveal the role of double excitations, we performed SH simulations with FOMO-CISD within the same active space, resulting in nine Slater determinants used to construct wave functions. These calculations resulted in a quantum yield (for the monomer) of $\sim$30% (29.8 $\pm$ 3.7% for 151 trajectories and 30.3 $\pm$ 5.3% for 76 trajectories). The corresponding $n\pi^*$ lifetime is 1092 fs. Thus, while inclusion of double excitations considerably increases the quantum yield (from $\sim$14% (CIS) to $\sim$30% (CISD) in the case of the full set of 151 trajectories), the $n\pi^*$ lifetime still remains long, $\sim$1 ps (it decreases from 1266 fs (CIS) to 1092 fs (CISD), see Fig. S6 for S_1 populations calculated with both methods). Expansion of the active space is therefore needed to obtain a shorter lifetime compatible with earlier works.[91,92,96]

Further, similarly to the case of the $\pi\pi^*$ excitation,[47] we observe smaller quantum yields when going from the monomer to the tetrameric models (Tab. 3). Specifically, the $n\pi^*$ quantum yields are $\sim$7–8% for models with $a = 5.5$ Å and tetramer 3.5 Å, and 0 for SAM 3.5 Å.

25

The reduction factor "monomer/tetramer" is ~ 2 (considering the batch of 151 trajectories). Compared to the $\pi\pi^*$ quantum yields, the $n\pi^*$ quantum yields are slightly higher, as is the case for the monomer (Tab. 3) (except for SAM 3.5 Å, for which $\Phi = 0$ in either case). Here, we should note that previously, for a dimeric SAM model with $a = 4.0$ Å, the opposite was found, *i.e.*, $\Phi_{n\pi^*} \approx 3\%$ and $\Phi_{\pi\pi^*} \approx 9\%$.[58] There can be several reasons responsible for this discrepancy, including different electronic structure methods (in terms of the size of the active space and allowed excitations), the use or disuse of the added potential,[61] and the size of the QM part. The understanding of this problem would require further simulations going beyond the scope of the present work.

Next, for the reactive trajectories, it is interesting to analyze which monomer undergoes isomerization. We note that, for the reactive trajectories, usually only one of the four monomers switches to the *cis* form (only three trajectories exhibit additional isomerizations caused by repopulation of excited states from the ground state). For tetramer 3.5 Å, out of 11 reactive trajectories, we find that 4, 1, 0, and 6 correspond to isomerization of monomers 1, 2, 3, and 4, respectively (see Fig. 1 for numbering of the monomers). Thus, for tetramer 3.5 Å there is a preference for isomerization of end molecules (1 and 4). For tetramer 5.5 Å, out of 12 reactive trajectories, 3, 3, 3, and 3 show isomerization of monomers 1, 2, 3, and 4, respectively. In this case, we find a uniform "distribution". However, the overall quantum yields of tetramers 3.5 and 5.5 Å are very similar (both $\sim 8\%$). Thus, despite the fact that every QM molecule can isomerize in tetramer 5.5 Å, it turns out that azobenzene isomerization ability is affected at $a = 5.5$ Å. For SAM 5.5 Å, out of 10 reactive trajectories, we find 4, 3, 2, and 1 trajectories with switching of monomer 1, 2, 3, and 4, respectively. In this case the "distribution" is asymmetric which can originate from too few members of the sample.

Finally, enlargement of the batch size from 76 trajectories to 151 trajectories, leads to the following changes in the quantum yields: -4.5% for monomer upon $n\pi^*$ excitation and -4.0% for monomer upon $\pi\pi^*$ excitation; $+2.7\%$ for tetramer 5.5 Å ($n\pi^*$) and -1.0% for

tetramer 5.5 Å ($\pi\pi^*$); +0.2% for SAM 5.5 Å ($n\pi^*$); and +1% for tetramer 3.5 Å ($n\pi^*$). For SAM 3.5 Å, no isomerization is observed irrespective of excitation ($n\pi^*$ or $\pi\pi^*$) and the batch size.

4   Conclusions

We studied nonadiabatic dynamics of tetrameric aggregates of azobenzene upon $n\pi^*$ excitation using the rAM1/FOMO-CIS electronic structure approach combined with the surface hopping scheme for modeling nonadiabatic dynamics. The *exciton dynamics* of the $n\pi^*$ excitons excited with visible light is the focus of the present study. These dynamics were revealed using the transition density matrix analysis.

We found that initial excitons (computed at the initial geometries from ground-state Langevin MD) are strongly localized. However, they undergo even further extremely ultrafast localization during first femtoseconds of nonadiabatic dynamics with a time constant of 6–7 fs. After that, the $n\pi^*$ excitons stay localized throughout the dynamics and normally no exciton transfer occurs between monomers while aggregates evolve in the $n\pi^*$ manifold. Only a few trajectories demonstrated the exciton transfer during dynamics in the $n\pi^*$ states. In addition, we observed that the exciton transfer may be realized through population of the higher lying $\pi\pi^*$ states or through upward hops from the ground state (reached, in turn, via internal conversion) to excited states.

The $n\pi^*$ *trans* $\rightarrow$ *cis* isomerization quantum yields are lower by a factor of about two for free / not strongly constrained tetramers than for the monomer, and no switching is observed for the most tightly packed model (SAM 3.5 Å). The $n\pi^*$ quantum yields for the aggregates are found to be slightly larger than the $\pi\pi^*$ quantum yields (obtained at the same level of theory in ref. 47).

Acknowledgement

Supporting Information Available

Mean NNCC and CNNC dihedral angles for initial geometries, examples of trajectories demonstrating exciton transfer, LE and CT curves, populations of the individual states, S_1 populations for the monomer calculated with FOMO-CIS and FOMO-CISD.

References

(1) Davydov, A. S. The theory of molecular excitons. *Soviet Physics Uspekhi* **1964**, *7*, 145–178.

(2) Kasha, M.; Rawls, H. R.; El-Bayoumi, M. A. The exciton model in molecular spectroscopy. *Pure Appl. Chem.* **1965**, *11*, 371–392.

(3) Hestand, N. J.; Spano, F. C. Expanded Theory of H- and J-Molecular Aggregates: The Effects of Vibronic Coupling and Intermolecular Charge Transfer. *Chem. Rev.* **2018**, *118*, 7069–7163.

(4) Ostroverkhova, O. Organic Optoelectronic Materials: Mechanisms and Applications. *Chem. Rev.* **2016**, *116*, 13279–13412.

(5) Mirkovic, T.; Ostroumov, E. E.; Anna, J. M.; van Grondelle, R.; Govindjee; Sc-

holes, G. D. Light Absorption and Energy Transfer in the Antenna Complexes of Photosynthetic Organisms. *Chem. Rev.* **2017**, *117*, 249–293.

(6) Yamauchi, M.; Yokoyama, K.; Aratani, N.; Yamada, H.; Masuo, S. Crystallization-Induced Emission of Azobenzene Derivatives. *Angew. Chem. Int. Ed.* **2019**, *58*, 14173–14178.

(7) Klajn, R. Immobilized azobenzenes for the construction of photoresponsive materials. *Pure Appl. Chem.* **2010**, *82*, 2247–2279.

(8) Valley, D. T.; Onstott, M.; Malyk, S.; Benderskii, A. V. Steric Hindrance of Photoswitching in Self-Assembled Monolayers of Azobenzene and Alkane Thiols. *Langmuir* **2013**, *29*, 11623–11631.

(9) Bandara, H. M. D.; Burdette, S. C. Photoisomerization in different classes of azobenzene. *Chem. Soc. Rev.* **2012**, *41*, 1809–1825.

(10) Ibrahim, A. R.; Khyasudeen, M. F.; Husband, J.; Alauddin, S. M.; Aripin, N. F. K.; Velayutham, T. S.; Martinez-Felipe, A.; Abou-Zied, O. K. p-Methoxy Azobenzene Terpolymer as a Promising Energy-Storage Liquid Crystal System. *J. Phys. Chem. C* **2021**, *125*, 22472–22482.

(11) Gahl, C.; Schmidt, R.; Brete, D.; McNellis, E. R.; Freyer, W.; Carley, R.; Reuter, K.; Weinelt, M. Structure and Excitonic Coupling in Self-Assembled Monolayers of Azobenzene-Functionalized Alkanethiols. *J. Am. Chem. Soc.* **2010**, *132*, 1831–1838.

(12) Malyar, I. V.; Titov, E.; Lomadze, N.; Saalfrank, P.; Santer, S. Photoswitching of azobenzene-containing self-assembled monolayers as a tool for control over silicon surface electronic properties. *J. Chem. Phys.* **2017**, *146*, 104703.

(13) Blayo, C.; Houston, J. E.; King, S. M.; Evans, R. C. Unlocking Structure–Self-Assembly

Relationships in Cationic Azobenzene Photosurfactants. *Langmuir* **2018**, *34*, 10123–10134.

(14) Titov, E.; Sharma, A.; Lomadze, N.; Saalfrank, P.; Santer, S.; Bekir, M. Photoisomerization of an Azobenzene-Containing Surfactant Within a Micelle. *ChemPhotoChem* **2021**, *5*, 926–932.

(15) Zakrevskyy, Y.; Titov, E.; Lomadze, N.; Santer, S. Phase diagrams of DNA–photosensitive surfactant complexes: Effect of ionic strength and surfactant structure. *J. Chem. Phys.* **2014**, *141*, 164904.

(16) Kasyanenko, N.; Lysyakova, L.; Ramazanov, R.; Nesterenko, A.; Yaroshevich, I.; Titov, E.; Alexeev, G.; Lezov, A.; Unksov, I. Conformational and phase transitions in DNA—photosensitive surfactant solutions: Experiment and modeling. *Biopolymers* **2015**, *103*, 109–122.

(17) Song, X.; Perlstein, J.; Whitten, D. G. Supramolecular Aggregates of Azobenzene Phospholipids and Related Compounds in Bilayer Assemblies and Other Microheterogeneous Media: Structure, Properties, and Photoreactivity1. *J. Am. Chem. Soc.* **1997**, *119*, 9144–9159.

(18) Baroncini, M.; Bergamini, G. Azobenzene: A Photoactive Building Block for Supramolecular Architectures. *Chem. Rec.* **2017**, *17*, 700–712.

(19) Moldt, T.; Brete, D.; Przyrembel, D.; Das, S.; Goldman, J. R.; Kundu, P. K.; Gahl, C.; Klajn, R.; Weinelt, M. Tailoring the Properties of Surface-Immobilized Azobenzenes by Monolayer Dilution and Surface Curvature. *Langmuir* **2015**, *31*, 1048–1057.

(20) Utecht, M.; Klamroth, T.; Saalfrank, P. Optical absorption and excitonic coupling in azobenzenes forming self-assembled monolayers: a study based on density functional theory. *Phys. Chem. Chem. Phys.* **2011**, *13*, 21608–21614.

(21) Titov, E.; Saalfrank, P. Exciton Splitting of Adsorbed and Free 4-Nitroazobenzene Dimers: A Quantum Chemical Study. *J. Phys. Chem. A* **2016**, *120*, 3055–3070.

(22) Titov, E. On the Low-Lying Electronically Excited States of Azobenzene Dimers: Transition Density Matrix Analysis. *Molecules* **2021**, *26*, 4245.

(23) Cocchi, C.; Moldt, T.; Gahl, C.; Weinelt, M.; Draxl, C. Optical properties of azobenzene-functionalized self-assembled monolayers: Intermolecular coupling and many-body interactions. *J. Chem. Phys.* **2016**, *145*, 234701.

(24) Cocchi, C.; Draxl, C. Understanding the effects of packing and chemical terminations on the optical excitations of azobenzene-functionalized self-assembled monolayers. *J. Phys.: Condens. Matter* **2017**, *29*, 394005.

(25) Titov, E.; Beqiraj, A. Exciton States of Azobenzene Aggregates: A First-Principles Study. *Adv. Theory Simul.* **2023**, *6*, 2200907.

(26) Barbatti, M.; Sen, K. Effects of different initial condition samplings on photodynamics and spectrum of pyrrole. *Int. J. Quantum Chem.* **2016**, *116*, 762–771.

(27) Titov, E. Effect of conformational disorder on exciton states of an azobenzene aggregate. *Phys. Chem. Chem. Phys.* **2022**, *24*, 24002–24006.

(28) Åke Andersson, J.; Petterson, R.; Tegnér, L. Flash photolysis experiments in the vapour phase at elevated temperatures I: spectra of azobenzene and the kinetics of its thermal cis-trans isomerization. *J. Photochem.* **1982**, *20*, 17–32.

(29) Vetráková, Ľ.; Ladányi, V.; Al Anshori, J.; Dvořák, P.; Wirz, J.; Heger, D. The absorption spectrum of cis-azobenzene. *Photochem. Photobiol. Sci.* **2017**, *16*, 1749–1756.

(30) Wang, J.; Huang, J.; Du, L.; Lan, Z. Photoinduced Ultrafast Intramolecular Excited-State Energy Transfer in the Silylene-Bridged Biphenyl and Stilbene (SBS) System: A Nonadiabatic Dynamics Point of View. *J. Phys. Chem. A* **2015**, *119*, 6937–6948.

(31) Stojanović, L.; Aziz, S. G.; Hilal, R. H.; Plasser, F.; Niehaus, T. A.; Barbatti, M. Nonadiabatic Dynamics of Cycloparaphenylenes with TD-DFTB Surface Hopping. *J. Chem. Theory Comput.* **2017**, *13*, 5846–5860.

(32) Nelson, T. R.; Ondarse-Alvarez, D.; Oldani, N.; Rodriguez-Hernandez, B.; Alfonso-Hernandez, L.; Galindo, J. F.; Kleiman, V. D.; Fernandez-Alberti, S.; Roitberg, A. E.; Tretiak, S. Coherent exciton-vibrational dynamics and energy transfer in conjugated organics. *Nat. Commun.* **2018**, *9*, 2316.

(33) Titov, E.; Humeniuk, A.; Mitrić, R. Exciton localization in excited-state dynamics of a tetracene trimer: a surface hopping LC-TDDFTB study. *Phys. Chem. Chem. Phys.* **2018**, *20*, 25995–26007.

(34) Zhang, S.; Zeng, Y.-P.; Wan, X.-J.; Xu, D.-H.; Liu, X.-Y.; Cui, G.; Li, L. Ultrafast exciton delocalization and localization dynamics of a perylene bisimide quadruple π-stack: a nonadiabatic dynamics simulation. *Phys. Chem. Chem. Phys.* **2022**, *24*, 7293–7302.

(35) Peng, W.-T.; Brey, D.; Giannini, S.; Dell'Angelo, D.; Burghardt, I.; Blumberger, J. Exciton Dissociation in a Model Organic Interface: Excitonic State-Based Surface Hopping versus Multiconfigurational Time-Dependent Hartree. *J. Phys. Chem. Lett.* **2022**, *13*, 7105–7112.

(36) Binder, R.; Wahl, J.; Römer, S.; Burghardt, I. Coherent exciton transport driven by torsional dynamics: a quantum dynamical study of phenylene-vinylene type conjugated systems. *Faraday Discuss.* **2013**, *163*, 205–222.

(37) Brüning, C.; Wehner, J.; Hausner, J.; Wenzel, M.; Engel, V. Exciton dynamics in perturbed vibronic molecular aggregates. *Struct. Dyn.* **2016**, *3*, 043201.

(38) Binder, R.; Lauvergnat, D.; Burghardt, I. Conformational Dynamics Guides Coher-

ent Exciton Migration in Conjugated Polymer Materials: First-Principles Quantum Dynamical Study. *Phys. Rev. Lett.* **2018**, *120*, 227401.

(39) Binder, R.; Burghardt, I. First-principles description of intra-chain exciton migration in an oligo(para-phenylene vinylene) chain. II. ML-MCTDH simulations of exciton dynamics at a torsional defect. *J. Chem. Phys.* **2020**, *152*, 204120.

(40) Mondelo-Martell, M.; Brey, D.; Burghardt, I. Quantum dynamical study of inter-chain exciton transport in a regioregular P3HT model system at finite temperature: HJ vs H-aggregate models. *J. Chem. Phys.* **2022**, *157*, 094108.

(41) Fernandez-Alberti, S.; Makhov, D. V.; Tretiak, S.; Shalashilin, D. V. Non-adiabatic excited state molecular dynamics of phenylene ethynylene dendrimer using a multiconfigurational Ehrenfest approach. *Phys. Chem. Chem. Phys.* **2016**, *18*, 10028–10040.

(42) Freixas, V. M.; White, A. J.; Nelson, T.; Song, H.; Makhov, D. V.; Shalashilin, D.; Fernandez-Alberti, S.; Tretiak, S. Nonadiabatic Excited-State Molecular Dynamics Methodologies: Comparison and Convergence. *J. Phys. Chem. Lett.* **2021**, *12*, 2970–2982.

(43) Cotton, S. J.; Miller, W. H. The Symmetrical Quasi-Classical Model for Electronically Non-Adiabatic Processes Applied to Energy Transfer Dynamics in Site-Exciton Models of Light-Harvesting Complexes. *J. Chem. Theory Comput.* **2016**, *12*, 983–991.

(44) Liang, R.; Cotton, S. J.; Binder, R.; Hegger, R.; Burghardt, I.; Miller, W. H. The symmetrical quasi-classical approach to electronically nonadiabatic dynamics applied to ultrafast exciton migration processes in semiconducting polymers. *J. Chem. Phys.* **2018**, *149*, 044101.

(45) Sangiogo Gil, E.; Granucci, G.; Persico, M. Surface Hopping Dynamics with the Frenkel Exciton Model in a Semiempirical Framework. *J. Chem. Theory Comput.* **2021**, *17*, 7373–7383.

33

(46) Sangiogo Gil, E.; Persico, M.; Granucci, G. Frenkel exciton photodynamics of self-assembled monolayers of azobiphenyls. *J. Chem. Phys.* **2022**, *157*, 161101.

(47) Titov, E. Exciton Localization and Transfer in Azobenzene Aggregates: A Surface Hopping Molecular Dynamics Study. *J. Phys. Chem. C* **2023**, *127*, 13678–13688.

(48) Plasser, F.; Granucci, G.; Pittner, J.; Barbatti, M.; Persico, M.; Lischka, H. Surface hopping dynamics using a locally diabatic formalism: Charge transfer in the ethylene dimer cation and excited state dynamics in the 2-pyridone dimer. *J. Chem. Phys.* **2012**, *137*, 22A514.

(49) Fernandez-Alberti, S.; Roitberg, A. E.; Kleiman, V. D.; Nelson, T.; Tretiak, S. Shishiodoshi unidirectional energy transfer mechanism in phenylene ethynylene dendrimers. *J. Chem. Phys.* **2012**, *137*, 22A526.

(50) Galindo, J. F.; Atas, E.; Altan, A.; Kuroda, D. G.; Fernandez-Alberti, S.; Tretiak, S.; Roitberg, A. E.; Kleiman, V. D. Dynamics of Energy Transfer in a Conjugated Dendrimer Driven by Ultrafast Localization of Excitations. *J. Am. Chem. Soc.* **2015**, *137*, 11637–11644.

(51) Nelson, T.; Fernandez-Alberti, S.; Roitberg, A. E.; Tretiak, S. Electronic Delocalization, Vibrational Dynamics, and Energy Transfer in Organic Chromophores. *J. Phys. Chem. Lett.* **2017**, *8*, 3020–3031.

(52) Titov, E.; Kopp, T.; Hoche, J.; Humeniuk, A.; Mitrić, R. (De)localization dynamics of molecular excitons: comparison of mixed quantum-classical and fully quantum treatments. *Phys. Chem. Chem. Phys.* **2022**, *24*, 12136–12148.

(53) Dong, M.; Babalhavaeji, A.; Samanta, S.; Beharry, A. A.; Woolley, G. A. Red-Shifting Azobenzene Photoswitches for in Vivo Use. *Acc. Chem. Res.* **2015**, *48*, 2662–2670.

(54) Beharry, A. A.; Sadovski, O.; Woolley, G. A. Azobenzene Photoswitching without Ultraviolet Light. *J. Am. Chem. Soc.* **2011**, *133*, 19684–19687.

(55) Bléger, D.; Hecht, S. Visible-Light-Activated Molecular Switches. *Angew. Chem. Int. Ed.* **2015**, *54*, 11338–11349.

(56) Kuntze, K.; Viljakka, J.; Titov, E.; Ahmed, Z.; Kalenius, E.; Saalfrank, P.; Priimagi, A. Towards low-energy-light-driven bistable photoswitches: ortho-fluoroaminoazobenzenes. *Photochem. Photobiol. Sci.* **2022**, *21*, 159–173.

(57) Titov, E.; Granucci, G.; Götze, J. P.; Persico, M.; Saalfrank, P. Dynamics of Azobenzene Dimer Photoisomerization: Electronic and Steric Effects. *J. Phys. Chem. Lett.* **2016**, *7*, 3591–3596.

(58) Rietze, C.; Titov, E.; Granucci, G.; Saalfrank, P. Surface Hopping Dynamics for Azobenzene Photoisomerization: Effects of Packing Density on Surfaces, Fluorination, and Excitation Wavelength. *J. Phys. Chem. C* **2020**, *124*, 26287–26295.

(59) Granucci, G.; Toniolo, A. Molecular gradients for semiempirical CI wavefunctions with floating occupation molecular orbitals. *Chem. Phys. Lett.* **2000**, *325*, 79–85.

(60) Dewar, M. J. S.; Zoebisch, E. G.; Healy, E. F.; Stewart, J. J. P. Development and use of quantum mechanical molecular models. 76. AM1: a new general purpose quantum mechanical molecular model. *J. Am. Chem. Soc.* **1985**, *107*, 3902–3909.

(61) Cusati, T.; Granucci, G.; Martínez-Núñez, E.; Martini, F.; Persico, M.; Vázquez, S. Semiempirical Hamiltonian for Simulation of Azobenzene Photochemistry. *J. Phys. Chem. A* **2012**, *116*, 98–110.

(62) Accomasso, D.; Granucci, G.; Persico, M. Singlet fission in covalent dimers of methylene-locked 1,3-diphenyl-isobenzofuran: semiclassical simulations of nonadiabatic dynamics. *J. Mater. Chem. A* **2021**, *9*, 21897–21909.

(63) The vdW parameters are taken from the oplsaa.prm file of TINKER 6.1 distribution. These parameters, in turn, are from "OPLS All-Atom Parameters for Organic Molecules, Ions, Peptides & Nucleic Acids, July 2008" as provided by W. L. Jorgensen, Yale University during June 2009.

(64) Cusati, T.; Granucci, G.; Persico, M.; Spighi, G. Oscillator strength and polarization of the forbidden $n \to \pi^*$ band of trans-azobenzene: A computational study. *J. Chem. Phys.* **2008**, *128*, 194312.

(65) Tully, J. C. Molecular dynamics with electronic transitions. *J. Chem. Phys.* **1990**, *93*, 1061–1071.

(66) Granucci, G.; Persico, M.; Toniolo, A. Direct semiclassical simulation of photochemical processes with semiempirical wave functions. *J. Chem. Phys.* **2001**, *114*, 10608–10615.

(67) Granucci, G.; Persico, M. Critical appraisal of the fewest switches algorithm for surface hopping. *J. Chem. Phys.* **2007**, *126*, 134114.

(68) Aguilera-Porta, N.; Corral, I.; Munoz-Muriedas, J.; Granucci, G. Excited state dynamics of some nonsteroidal anti-inflammatory drugs: A surface-hopping investigation. *Comput. Theor. Chem.* **2019**, *1152*, 20–27.

(69) Nelson, T. R.; White, A. J.; Bjorgaard, J. A.; Sifain, A. E.; Zhang, Y.; Nebgen, B.; Fernandez-Alberti, S.; Mozyrsky, D.; Roitberg, A. E.; Tretiak, S. Non-adiabatic Excited-State Molecular Dynamics: Theory and Applications for Modeling Photophysics in Extended Molecular Materials. *Chem. Rev.* **2020**, *120*, 2215–2287.

(70) Nottoli, M.; Cupellini, L.; Lipparini, F.; Granucci, G.; Mennucci, B. Multiscale Models for Light-Driven Processes. *Annu. Rev. Phys. Chem.* **2021**, *72*, 489–513.

(71) Qiu, T.; Climent, C.; Subotnik, J. E. A Practical Approach to Wave Function Prop-

agation, Hopping Probabilities, and Time Steps in Surface Hopping Calculations. *J. Chem. Theory Comput.* **2023**, *19*, 2744–2757.

(72) McWeeny, R. Some Recent Advances in Density Matrix Theory. *Rev. Mod. Phys.* **1960**, *32*, 335–369.

(73) Tretiak, S.; Mukamel, S. Density Matrix Analysis and Simulation of Electronic Excitations in Conjugated and Aggregated Molecules. *Chem. Rev.* **2002**, *102*, 3171–3212.

(74) Plasser, F.; Lischka, H. Analysis of Excitonic and Charge Transfer Interactions from Quantum Chemical Calculations. *J. Chem. Theory Comput.* **2012**, *8*, 2777–2789.

(75) Nogueira, J. J.; Plasser, F.; González, L. Electronic delocalization, charge transfer and hypochromism in the UV absorption spectrum of polyadenine unravelled by multiscale computations and quantitative wavefunction analysis. *Chem. Sci.* **2017**, *8*, 5682–5691.

(76) Ishizaki, A.; Fleming, G. R. Quantum superpositions in photosynthetic light harvesting: delocalization and entanglement. *New Journal of Physics* **2010**, *12*, 055004.

(77) Hegger, R.; Binder, R.; Burghardt, I. First-Principles Quantum and Quantum-Classical Simulations of Exciton Diffusion in Semiconducting Polymer Chains at Finite Temperature. *J. Chem. Theory Comput.* **2020**, *16*, 5441–5455.

(78) Herbert, J. Visualizing and Characterizing Excited States from Time-Dependent Density Functional Theory. *ChemRxiv* **2023**, DOI: 10.26434/chemrxiv–2023–gnh1v.

(79) Clark, T. B. P.; Maestro, A. D. Moments of the inverse participation ratio for the Laplacian on finite regular graphs. *J. Phys. A: Math. Theor.* **2018**, *51*, 495003.

(80) Scholes, G. D. Limits of exciton delocalization in molecular aggregates. *Faraday Discuss.* **2020**, *221*, 265–280.

(81) Bell, R. J. The dynamics of disordered lattices. *Rep. Prog. Phys.* **1972**, *35*, 1315.

(82) Thouless, D. Electrons in disordered systems and the theory of localization. *Phys. Rep.* **1974**, *13*, 93–142.

(83) Wegner, F. Inverse participation ratio in $2+\varepsilon$ dimensions. *Z. Phys. B: Condens. Matter* **1980**, *36*, 209–214.

(84) Bell, R. J.; Dean, P. Atomic vibrations in vitreous silica. *Discuss. Faraday Soc.* **1970**, *50*, 55–61.

(85) Bell, R. J.; Dean, P.; Hibbins-Butler, D. C. Localization of normal modes in vitreous silica, germania and beryllium fluoride. *J. Phys. C: Solid State Phys.* **1970**, *3*, 2111.

(86) Alfonso Hernandez, L.; Nelson, T.; Gelin, M. F.; Lupton, J. M.; Tretiak, S.; Fernandez-Alberti, S. Interference of Interchromophoric Energy-Transfer Pathways in π-Conjugated Macrocycles. *J. Phys. Chem. Lett.* **2016**, *7*, 4936–4944.

(87) Ondarse-Alvarez, D.; Kömürlü, S.; Roitberg, A. E.; Pierdominici-Sottile, G.; Tretiak, S.; Fernandez-Alberti, S.; Kleiman, V. D. Ultrafast electronic energy relaxation in a conjugated dendrimer leading to inter-branch energy redistribution. *Phys. Chem. Chem. Phys.* **2016**, *18*, 25080–25089.

(88) Stewart, J. J. P. MOPAC 2002, Fujitsu Ltd., Tokyo, Japan.

(89) Rackers, J. A.; Wang, Z.; Lu, C.; Laury, M. L.; Lagardère, L.; Schnieders, M. J.; Piquemal, J.-P.; Ren, P.; Ponder, J. W. Tinker 8: Software Tools for Molecular Design. *J. Chem. Theory Comput.* **2018**, *14*, 5273–5289.

(90) Fliegl, H.; Köhn, A.; Hättig, C.; Ahlrichs, R. Ab Initio Calculation of the Vibrational and Electronic Spectra of trans- and cis-Azobenzene. *J. Am. Chem. Soc.* **2003**, *125*, 9821–9827.

(91) Cantatore, V.; Granucci, G.; Persico, M. Simulation of the $\pi \rightarrow \pi^*$ photodynamics of

azobenzene: Decoherence and solvent effects. *Comput. Theor. Chem.* **2014**, *1040-1041*, 126–135.

(92) Gámez, J. A.; Weingart, O.; Koslowski, A.; Thiel, W. Cooperating Dinitrogen and Phenyl Rotations in trans-Azobenzene Photoisomerization. *J. Chem. Theory Comput.* **2012**, *8*, 2352–2358.

(93) Yu, L.; Xu, C.; Lei, Y.; Zhu, C.; Wen, Z. Trajectory-based nonadiabatic molecular dynamics without calculating nonadiabatic coupling in the avoided crossing case: trans ↔ cis photoisomerization in azobenzene. *Phys. Chem. Chem. Phys.* **2014**, *16*, 25883–25895.

(94) Yu, J. K.; Bannwarth, C.; Liang, R.; Hohenstein, E. G.; Martínez, T. J. Nonadiabatic Dynamics Simulation of the Wavelength-Dependent Photochemistry of Azobenzene Excited to the nπ^* and $\pi\pi^*$ Excited States. *J. Am. Chem. Soc.* **2020**, *142*, 20680–20690.

(95) Todd J. Martínez, personal communication.

(96) Yu, J. K.; Bannwarth, C.; Hohenstein, E. G.; Martínez, T. J. Ab Initio Nonadiabatic Molecular Dynamics with Hole–Hole Tamm–Dancoff Approximated Density Functional Theory. *J. Chem. Theory Comput.* **2020**, *16*, 5499–5511.

(97) Cantatore, V.; Granucci, G.; Rousseau, G.; Padula, G.; Persico, M. Photoisomerization of Self-Assembled Monolayers of Azobiphenyls: Simulations Highlight the Role of Packing and Defects. *J. Phys. Chem. Lett.* **2016**, *7*, 4027–4031.

(98) Ladányi, V.; Dvořák, P.; Al Anshori, J.; Vetráková, Ľ.; Wirz, J.; Heger, D. Azobenzene photoisomerization quantum yields in methanol redetermined. *Photochem. Photobiol. Sci.* **2017**, *16*, 1757–1761.

TOC Graphic